In this chapter, we present the geometrical model used to simulate the ideal emission signal of the planet received by a distant observer at any given location, as well as the methods used to determine the global characteristics of the climate and to analyze the thermal light curve of the planet. The model transforms emission flux maps into the point-like signal of the planet and it is capable of calculating global parameters as the effective temperature or the Bond albedo to constrain the characteristics of the planetary climate. Then, we perform the analysis of the light curve obtained from the model with the aim of discussing the reliability of the parameters retrieved from the signal in each case. This chapter is organized as follows: the geometrical model is described in Section 2.1, the parameters used to typify the climate are presented in Section 2.2, and the methods of analysis of the signal are given in Section 2.3.

Geometrical Model

Our mathematical model uses a series of matrices of flux maps (emission flux as a function of longitude, latitude and time) as input data. We have used top-of-the-atmosphere (TOA) thermal emission flux maps with the purpose of building the infrared emission signal of the planet, however, other types of input data can be implemented by the model. Besides of the computation of the point-like emission from the TOA, the model can be applied to obtain global mean values as the global mean temperature at a certain altitude, the global cloud fraction, the albedo or the effective temperature, and it can also be adapted to cover specific regions of the planet. Each matrix point is defined as the mean value in the center of each grid cell, then the matrices are transformed in several steps:

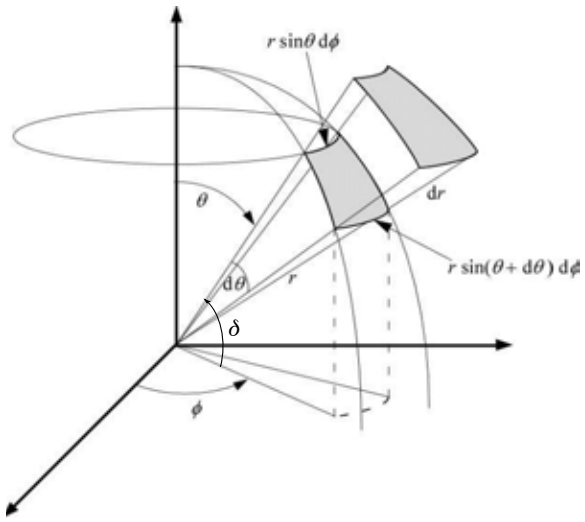

FIGURE 2.1 Spherical coordinates, where r is the radius of the sphere, θ and ϕ (longitude) are the spherical angles and δ is the geographical latitude.

i) Spherical maps.– According to the space resolution, the data matrices are converted into spherical maps by a transformation of the area $S_{i,j}$ of each grid cell. Defining $dS_{i,j}$ as the spherical elementary area (Fig. 2.1), $S_{i,j}$, the area of each grid cell can be calculated as:

$$\overrightarrow{dS}_{(i,j)} = R^2 \sin\theta \, d\theta \, d\phi \cdot \hat{r} \tag{2.1}$$

$$S_{i,j} = \int R^2 \cos\delta \, d\delta \, d\phi \tag{2.2}$$

$$S_{i,j} = R^2 \cdot (sin\delta_{i+1} - sin\delta_i) \cdot (\phi_{j+1} - \phi_j) \tag{2.3}$$

where (δ_i, δ_{i+1}) and (ϕ_j, ϕ_{j+1}) are the latitude and longitude limits of the each grid cell. For further calculations, we define the magnitude $a_{i,j}$, the unitary elementary as:

$$a_{\mathrm{i,j}} = (sin\delta_{i+1} - sin\delta_i) \cdot (\phi_{j+1} - \phi_j) \tag{2.4}$$

ii) Planetary position.– The position of the planet in the orbit is specified by the date, whereas the time is given either in Universal Time (UT) or by the location of the sub-stellar point, that can be obtained from the ephemeris. The

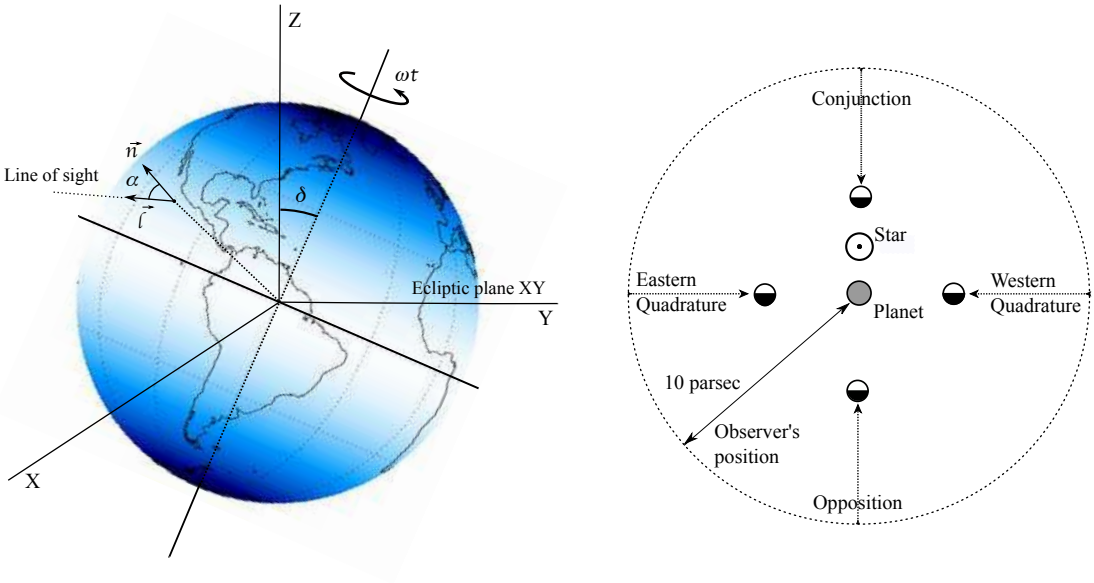

Figure 2.2 *Left:* Planetary configuration. *Right:* Schematic positions of the observers respect to the planet at the initial time: opposition, western quadrature, conjunction and eastern quadrature. The correspondent planetary phase seen by the observer is shown at the tip of the arrow pointing from the observer's position to the planet.

ephemeris implemented in the model are taken from the Jet Propulsion Laboratory (JLP) Horizons Ephemeris System, that adjusts the equations of motion to highly accurate measurements of planetary positions[1].

iii) Observer's position.– The coordinates of the observer are defined by the position of the sub-observer's point and the distance to the planet. To illustrate several simultaneous planet-observer geometries, we have defined observer positions by equatorial coordinates at a radius distance of 10 pc. In order to interpret the variation of the Earth emission in relation with the geographic features and the climate, it is relevant to locate the sub-observer point by its geographic coordinates: the equivalent of the declination angle on the planetary surface gives the latitude

[1]http://ssd.jpl.nasa.gov/?horizons

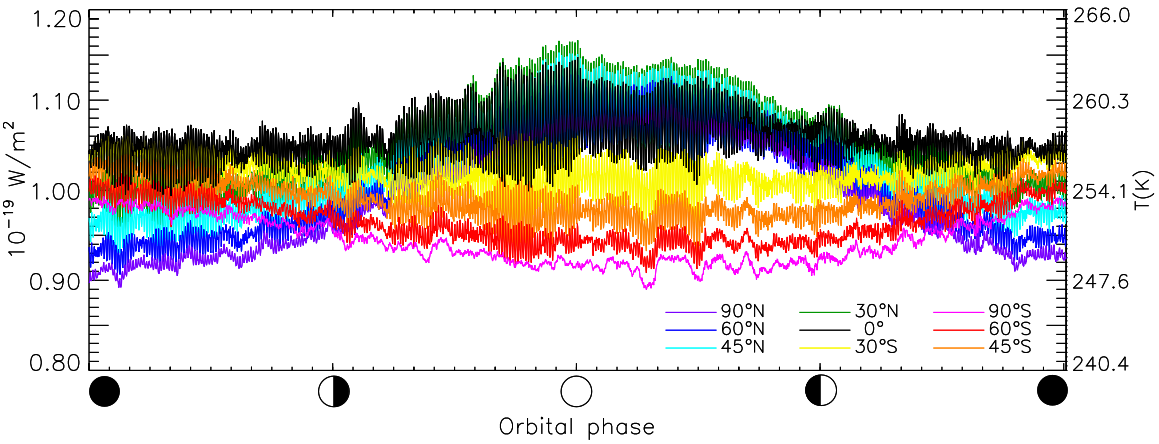

FIGURE 2.3 Earth orbital light curve. The colours indicate the latitude of the sub-observer point and the orbital phases correspond to an equatorial observer at opposition during northern winter (black line).

of the sub-observer point, which remains constant along the orbit. The latitude remains constant with time because precession and nutation are negligible during an orbit, and its longitude ϕ varies with time as $\phi(t) = \phi(t_0) - \omega t$, ω being the rotation rate of the Earth (with the exceptions of the polar cases where the planetary geometry does not change with time); therefore, we can define the sub-observer point by its latitude and its longitude at a given time.

The initial time is set to January 1, 0:00 UT of the year considered, then we use four different initial longitudes $\phi(t_0)$: the meridian of the sub-stellar point, the morning terminator, the meridian of the anti-stellar point and the evening terminator. We call these initial observing geometries conjunction (C), western quadrature (WQ), opposition (O) and eastern quadrature (EQ), respectively, although these terms should normally apply exclusively to an observer located in the ecliptic plane. Figure 2.2 represents a simplified scheme of the observers's positions used in this work. Previous studies ([e.g] Cowan et al. (2012)) define the planetary position in the orbit respect to the observer according to an inferior planet configuration. Because our study compares different views of the planet at the same moment, we have preferred to use an equivalent notation: we define

the observers's positions after a superior planet configuration. At the initial time, opposition designates an observer placed at a phase angle $\gamma = 180^o$, being midnight at the planetary disk Central Meridian (CM). An the observer is at conjunction when the planetary phase angle is $\gamma = 0^o$ (midday at CM). And therefore, western quadrature and eastern quadrature correspond to positions at $\gamma = 270^o$ and $\gamma = 90^o$, respectively. As the planet orbits around the star, its phase angle respect to the observer changes. For this matter, each observer is named after the position they have respect to the planet at the initial time of observation. In summary, the observers are placed respect to the equatorial plane, the sub-observer position over the planet is specified by the latitude of the sub-observer's point and by local hour at the CM.

It is important to note two facts: firstly, each observer sees the planet at a certain local hour during a whole rotation period, and secondly, observers placed at the same latitude but different longitudes see the same region of the planet at different local hours (i.e. if the (O) observer sees a given region of the planet during the winter midnight and the summer noon, the (C) observer sees the same region during the winter noon and the summer midnight). There is an exception for the polar views, where the observer sees the same hemisphere of the planet along the time of observation. In the need of a reference for time for this case, we define the "local hour" at a polar latitude according to the Universal Time (UT). In this case, the seasonal variability and the diurnal variability (daily change in temperature in a certain region) produce the variation of the signal and not the changing of the planetary view (rotational variability).

iv) Point-like signal.– In general, the flux received at a distance d is related to the flux emitted by the source as $F_{obs}(t) = \frac{R^2}{d^2} F_e$, where R^2 is in this case the radius of the planet. Specifically, at any moment, the planetary disk towards the observer is determined by the sub-observer point and the contribution of each point to the total flux is given by the Lambert's cosine law (Eq. 2.5) as the projection of the specific intensity of radiation into the direction of the observer, $I_r \cos \alpha_{i,j}(t)$, where $I^r_{i,j}$ is the specific intensity of radiation normal to the emission surface and $\alpha_{i,j}(t)$ is the angle between the surface normal and the observer's line of sight at

a time t. The cosine of this angle is calculated at any time by the dot product between the normal to the surface and the sub-observer's point vector, where the latter is defined by its geographical coordinates, as previously mentioned (Fig 2.2):

$$F_{i,j}(t) = \int I^n_{i,j} \cos\alpha_{i,j}(t)\, \mathrm{d}\Omega \tag{2.5}$$

In the model, the flux $F_{obs}(t)$ received at a distance d and at a time t is given by the sum of the contribution of each cell (i, j) in the solid angle towards the observer by:

$$F_{\mathrm{obs}}(t) = \frac{1}{d^2} \sum_{i,j} \left[a_{i,j} \cdot \cos\alpha_{i,j}(t) \cdot \left(\frac{F_{i,j}(t)}{\pi} \right) \right], \tag{2.6}$$

where $a_{i,j}$ is the area of each grid cell (Eq. 2.4), $F_{i,j}(t)$ is the emission flux value of each grid cell and $F_{i,j}(t)/\pi$ is the correspondent specific intensity in the Lambertian approximation. As a result, a flux time series is obtained with the time resolution of the input sequence.

v) Limb Darkening.– In order to convert the TOA flux into the disk-integrated flux received by a distant observer, we have previously assumed an isotropic (Lambertian) distribution of specific intensities at the TOA. The Lambertian emission is only dependent on directionality by the $\cos\alpha$, being α the viewing angle respect to the surface normal (Eq. 2.6). However, the specific intensities are not isotropic, but they produce a darkening or brightening effect towards the limb of the planetary disk depending on the thermal structure, the composition of the atmosphere, the emission wavelength and the geometry of observation. The deviations from the isotropic case can be classified into four components:

a) Horizontal inhomogeneities produced by the variation of the nature of the source and its emissivity. For instance, a parcel of desert emits more energy than the same area of ocean.

b) Vertical variations are related to the temperature profile and to the extinction of the atmosphere. In the first case, the contribution function that depends on the

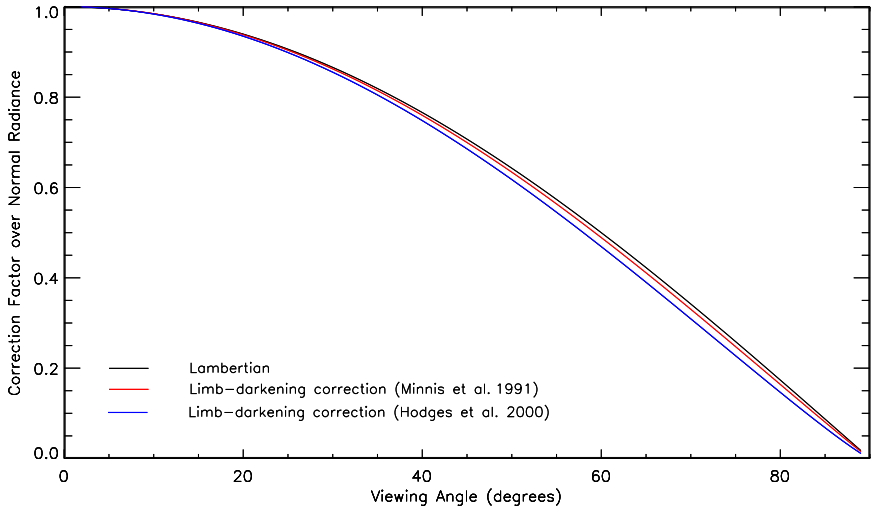

FIGURE 2.4 Correction factor L(α): radiance over normal radiance. Comparison between the Lambertian emission (black), the mean limb-darkening correction from Minnis et al. (1991) (red) and from Hodges et al. (2000) (blue).

wavelength band of observation, indicates the height of the emission layer in the atmosphere. In the second case, the emission is scattered and absorbed by the air mass along its path, depending on the emission wavelength and on the components of the atmosphere (aerosols, H_2O, O_2, etc.). Smith et al. (1994) studied the limb darkening in the broadband of (5-50) μm using the scanning radiometer data of the Earth Radiation Budget Experiment (ERBE)[2], reporting a limb brightening for winter polar nights as a result of night-time atmospheric temperature inversion.

c) Temporal fluctuations are produced by the daily and seasonal changes in the atmospheric profile and by the presence of clouds that partially absorb the radiation. Brooks & Fenn (1989) observed a difference between the daytime and the night-time limb-darkening, which is amplified in the case of surfaces with large diurnal temperature cycles (i.e Sahara desert). This effect also changes along the year. Peculiarly, the fluctuations are less marked during summer than during winter, being

[2]http://science.larc.nasa.gov/erbe/

specially stronger for the Northern Hemisphere over the Southern one. This result is explained by the fact that during summer, the large water vapor contain and the convection clouds in the atmosphere mask the strong diurnal temperature cycle of the surface. This behavior is amplified during the Northern summer because the large masses of land produce higher temperatures and therefore a larger fraction of convection clouds.

d) Angular variations are due to the directionality of both the emission and the extinction. The light from the limb of the planetary disk suffers a larger atmospheric absorption as it travels a longer path through the atmosphere than in the normal direction. Limb-darkening is also produced by geometric effects dependent on the position of the observer, for instance in a cloudy day, there is a higher probability of seeing the surface at nadir and the cloud tops at the limb.

The attenuation of the emission towards the limb of the planet is the result of the combination of these four effects. In the case of the Earth, the resemblance of limb-darkening parameterizations for specific conditions of the atmosphere, allows to built several mean models by averaging over latitude, time and surface types. The models establish a correction factor $L(\alpha)$ over the radiance normal to the surface in function of the viewing angle:

$$I(\alpha) = I_n \cdot L(\alpha) \tag{2.7}$$

where α is the viewing angle respect to the surface normal and I_n is the radiance at normal. Minnis et al. (1991) derived the empirical function:

$$L(\alpha) = \begin{cases} 1 & \text{if } \alpha < 11^\circ \\ b + a \ln(\cos\alpha) & \text{otherwise} \end{cases} \tag{2.8}$$

where $a = 0.03247$ and $b = 1.000602$. However Hodges et al. (2000) find that this correction is not sufficient, probably due to the lack of clouds or aerosols in the radiative models used for the numerical calculation and gives a correction with

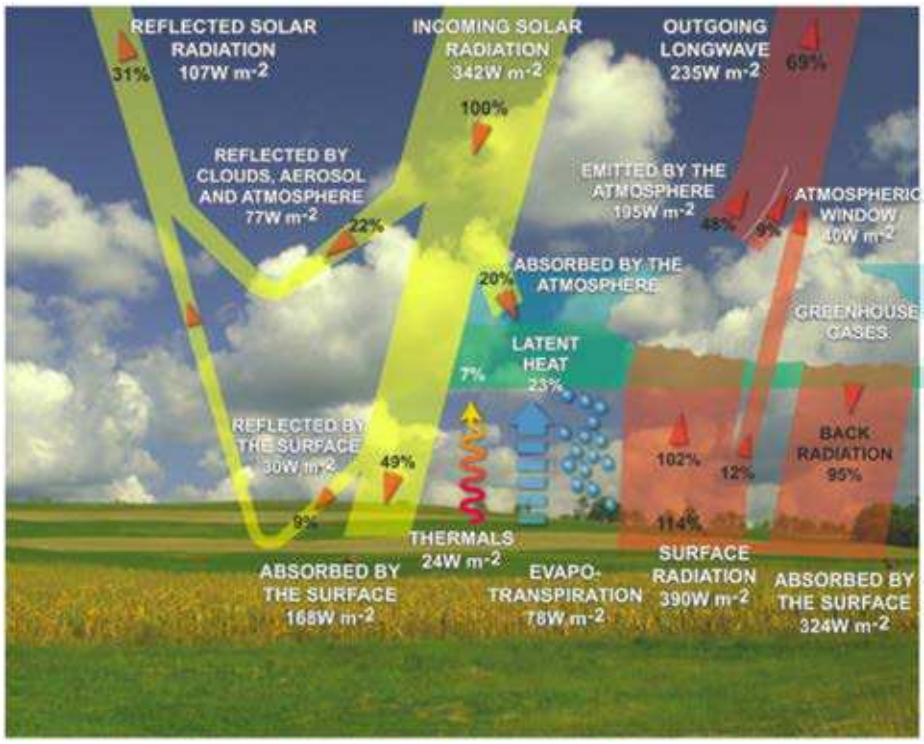

Figure 2.5 Earth radiation budget scheme.

$a = 0.09$ that it is in agreement with satellite measurements by GMS-4 and GOES-7. Figure 2.4 compares the Lambertian factor applied in this work and the correction factor for the mean limb-darkening models previously mentioned. Finally we have found that the limb-darkening corrections produce an attenuation of only (1.5±0.02)% for the model of Minnis et al. (1991) and an attenuation of (4±0.1)% for the model of Hodges et al. (2000) over the point-like signal derived by a Lambertian approximation. Thus, we conclude that the Lambertian approximation is valid to model the thermal point-like signal of an Earth-like planet.

2.2 Climate parameterization

2.2.1 Radiation Budget

The climate of an Earth-like planet is governed by the temperature of the surface, the atmosphere and the oceans, which in turn depend on the balance of energy fluxes. Considering the atmosphere as a whole, we can express the radiative balance equation as the equilibrium between the energy absorbed and the energy emitted by the planet.

The most fundamental sources of energy are the absorption of stellar radiation and the gravitational energy produced by the cooling of the planet, however this latter is negligible before the incoming energy from the star. The Solar mean radiative flux at Earth' distance is termed by the Solar constant $F_{\odot} = L/4\pi d_P^2 = 1366$ W/m^2, where L is the solar luminosity and d_P is the mean distance between the planet and the star (1UA), the actual flux varies along the seasons due to the eccentricity of the orbit. The mean incoming radiation is defined by the energy received by the illuminated side of the planet, which can be approximated by a disk of area πR_P^2. Planets do not behave like perfect blackbodies but they reflect part of the incoming energy. The ratio between the incoming and the reflected energies is represented by the Bond albedo A. The outgoing flux is expressed as the emission of a blackbody that radiates at the equilibrium temperature of the planet, also called effective temperature T_{eff}:

$$\pi R^2 (1 - A) F_S = 4\pi R^2 \sigma T_{eff}^4 \tag{2.9}$$

where R is the radius of the planet, σ is the Stefan-Boltzmann constant. In the case of the Earth, T_{eff} is $\simeq 255$ K and the emission of a blackbody at this temperature has a maximum at 11 μm which lies in the thermal (or longwave) infrared range (Fig 2.6), whereas the Sun emits primarily in the shortwave range (0.1- 5.0 μm). The effective temperature of the planet differs from its mean surface temperature ($T_S \simeq 288$ K), because of the action of the atmosphere. This effect, known as the greenhouse effect, works as follows: first, the radiation emitted by the surface is partially absorbed by the atmospheric compounds such as water vapor and carbon dioxide, and then these species warm up and re-emit the radiation to the atmosphere, warming the air around them. This mechanism is responsible of the temperature

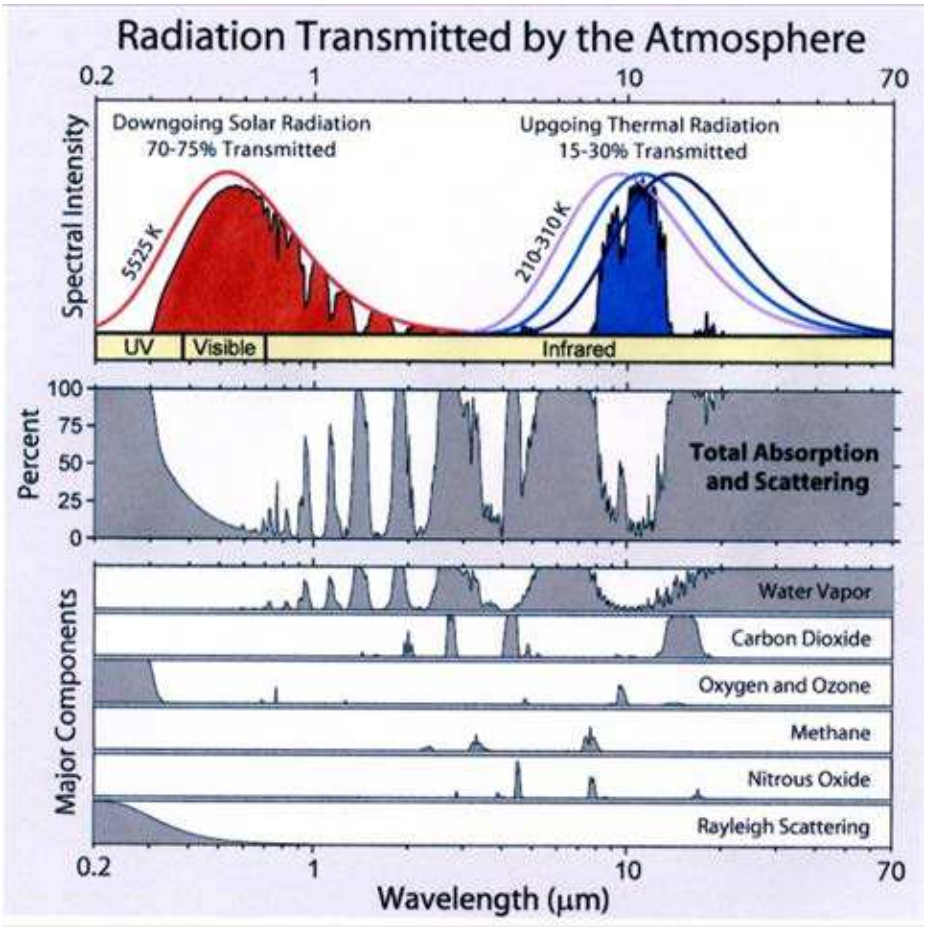

Figure 2.6 Transmittance of the Earth atmosphere and contributions of greenhouse gases. From Vázquez et al. (2010).

difference by trapping part of the infrared radiation in the atmosphere. It is termed by greenhouse parameter as:

$$\sigma T_{eff}^4 = (1-g)\sigma T_S^4 \tag{2.10}$$

Figure 2.6 illustrates the atmospheric transmittance of the atmosphere and the contribution of the most relevant greenhouse gases. We can see that water vapor is

responsible of most of the energy absorption and are a key factor in the study of the thermal emission of Earth-like planets. In the model, H_2O clouds are classified in two main groups depending on their response to radiation:

i) Low-level clouds are formed by water droplets and their bases lie below 2 km. They have a mean temperature at the top of $\simeq$ 280 K, a high optical depth in the shortwave range (4.7 at 0.6 μm), and a mean surface coverage of $\simeq$ 40 %.

ii) High-level clouds are formed by ice-crystals and lie above 6 km. They have a mean temperature at the top of $\simeq$ 227 K, a low optical depth in the shortwave range (2.2 at 0.6 μm), and a mean surface coverage of $\simeq$ 15 %. We have also included in this group vertically developed clouds. Although, they are formed mainly at low latitudes from thermal convection or frontal lifting, accumulating large amounts of energy through the condensation of water vapor, they can grow up to 12 km, thus they present similar properties to high clouds, having very cold cloud tops and absorbing most of the energy from below.

Low-level clouds have a pronounced effect in the planetary albedo, because of their large coverage fraction and high optical depth, they reflect 90 % of the incident solar energy and as a consequence the atmosphere below them is colder. At the same time, they re-emit the energy from the surface upwards at their top temperature, which does not differ considerably from the surface temperature, and they have a negligible greenhouse effect. On the contrary, high-clouds are not relevant to the albedo of the planet but have an important role on the greenhouse effect, they do not emit much radiation upwards as their cloud tops are very cold, then as a result, they block the surface emission, warming the atmosphere below them (Kitzmann et al., 2010, 2011).

Our aim is to infer certain characteristics of the planet from its thermal light curve. The brightness temperature of the planet can be determined from the thermal emission of the planet received by a distant observer ([e.g.]Gaidos & Williams (2004); Moskovitz et al. (2009); Cowan et al. (2012)): the flux F_e from a planetary disk can

be obtained by the integration of the Planck's law in the spectral band and in the solid angle of the observation:

$$F_e = \int_{\lambda_a}^{\lambda_b} \int_h B_\lambda(T_b)\, \mathrm{d}\Omega \tag{2.11}$$

where B_λ is the Planck's law, λ_a and λ_b are the limits of the spectral band, $d\Omega$ is the solid angle and h denotes the hemisphere exposed. As our spectral band of observation (5-50 μm) covers the whole emission of the planet, we can suppose the TOA-flux is bolometric and relate it to the global T_{eff} by $F_e \simeq \sigma T_{eff}^4$. Finally, the effective temperature of the planet is obtained relating Equation (2.11) with Equation (2.6) that relates the flux emitted by the planet with the flux received by the observer. Once the effective temperature is determined from the flux received and knowing the star incident flux at the mean planetary distance, the albedo (A) can be obtained from Eq. 2.9.

In addition, we can use the model information to derive some characteristics of its climate. The normalized greenhouse parameter g_N accounts for the fractional part of the thermal radiation that is absorbed and re-radiated back by the atmosphere, it depends on the wavelength range and on the difference between the mean surface flux obtained from the model and the mean TOA all-sky flux, supposing the flux is bolometric:

$$g_N^\lambda = \frac{F_s^\lambda - F_{TOA}^\lambda}{F_s^\lambda} \simeq \frac{\sigma T_{sur}^4 - \sigma T_{eff}^4}{\sigma T_{sur}^4} \tag{2.12}$$

where T_{sur} is the surface temperature, that is determined from the GCM data. The Cloud Radiative Forcing (CRF) quantifies the thermal emission absorption by the clouds. It is given by the difference between the emission for average conditions ($F_{all-sky}$) and cloud-free conditions (F_{clear}) at TOA:

$$CRF = F_{all-sky}^{TOA} - F_{clear}^{TOA} \tag{2.13}$$

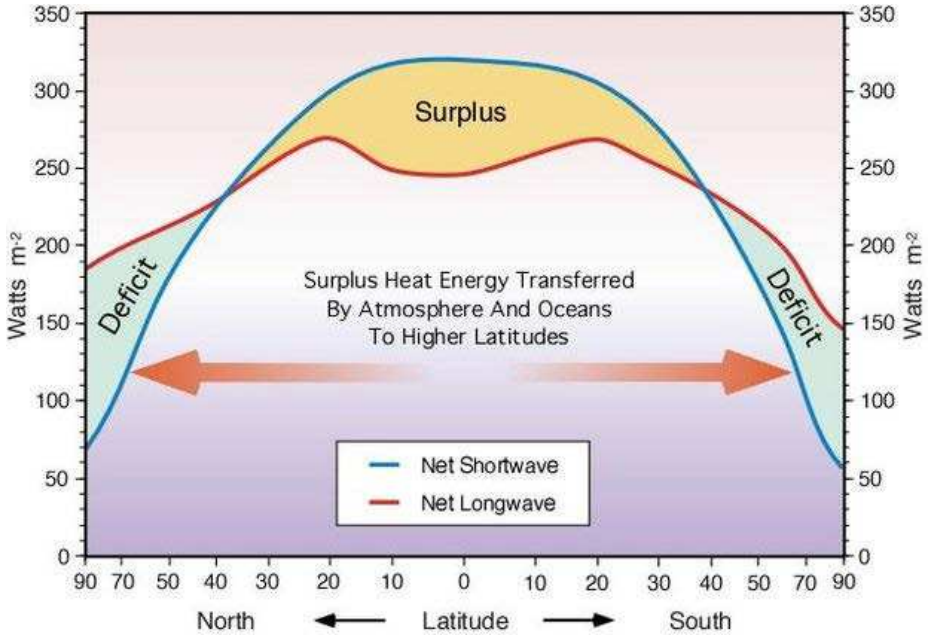

FIGURE 2.7 Earth net heat transport. The relations between the incoming (shortwave) radiation and the emitted (longwave) energy produce a net transport of heat.

In Section 5.2 and Section **??**, we have calculated T_{eff}, T_S, g_N, A, and CRF for our set of terrestrial planets and water worlds respectively, in order to typify the variety of their global properties and climates.

2.2.2 Circulation of the atmosphere

The incoming radiation is not the same for every point of the planet but it depends on the angle of incidence of the solar rays. Because of the sphericity of the planet, high latitudes receive less energy than low ones. There is also an insolation variation along the orbit, produced by the obliquity of the planet. In the case of the Earth, the rotation axis is tilted 23.5° respect to the normal to its orbital plane. For this reason, the subsolar point is not fixed at the equator along the orbit, but it moves inside the intertropical band, 23.5° north and south the equator, producing the seasons. The track followed by the subsolar point during one rotation is called thermal equator and

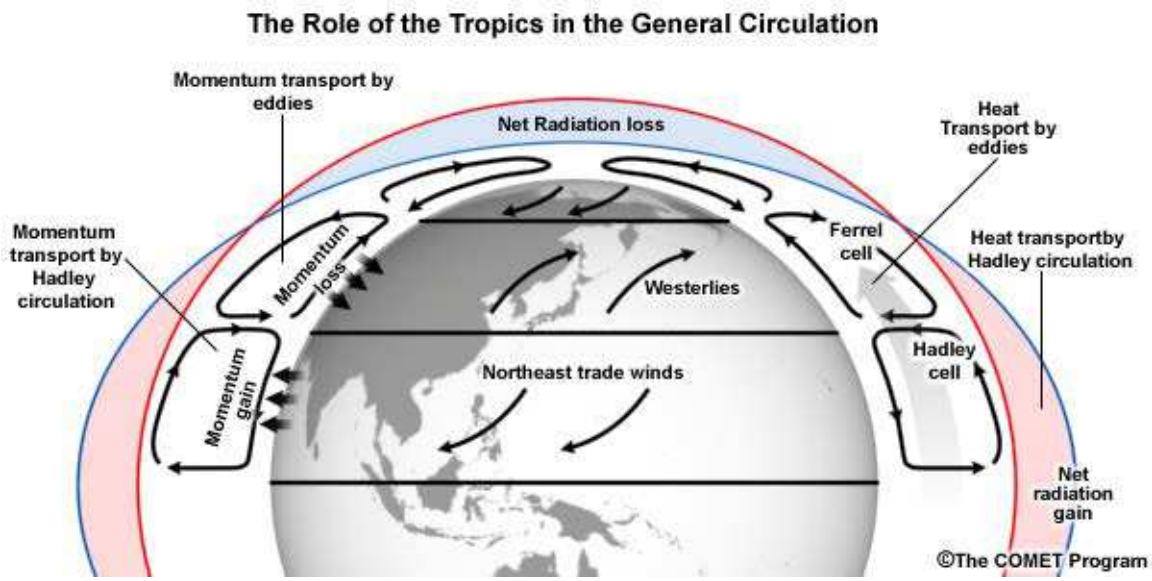

Figure 2.8 Earth atmospheric circulation and heat transport.

it is the place where the main circulation patterns of the atmosphere converge. The latitudinal variation on the energy over the planet is one of the main agents of the atmospheric circulation (along with the rotation rate, Section 2.2.3). The tropics, the region below 23.5° latitude, receive and emit more radiation than the poles, however the relation between the incoming and the outgoing energy is different, there is an excess of heat in the tropics and a deficit in the poles, as it is shown in Figure 2.7. As a consequence of this temperature gradient, heat is transported polewards by three main mechanisms:

i) Large scale circulation of the atmosphere.– In the case of the Earth, three latitudinal air cells are stablished in each hemisphere (Fig 2.8), the Hadley cell (0°-30° latitude), the Ferrel cell (30°- 60°) and the Polar cell (60°- 90°) . The Hadley cell is the most important circulation pattern, some slow rotating bodies, such as Venus and Titan, exhibit a single large cell in each hemisphere. On the contrary, in Earth, the Hadley cell extends from the thermal equator to 30° latitude. At the thermal equator, warm moist air rises to the tropopause creating a cloudy band called

Intertropical Convergence Zone (ITCZ), then the air is carried poleward and descends at about 30° latitude, part of the air moves back to the equator at the surface level creating the trade winds. The Ferrel Cell is not a closed loop driven by convection currents, but it is the result of the eddy circulations (high and low pressure regions) of the mid-latitudes, it extends from the 30° to 60° latitude and acts as a zone of mixing between the Polar and the Hadley cells. At 60° latitude in the polar cell, the air is moist and warm enough to be risen to the top of troposphere again and carried poleward, it descends at the cold and dry conditions of the polar latitude, and then finally it is driven southwards by the polar easterlies.

ii) Large scale circulation of the oceans.– In the oceans, the circulation is divided in two types of currents, surface currents and deep currents. Surface currents are driven by winds and modified by the Ekman transport, by which the direction of the ocean current is deflected in an angle to the stress of the wind, dependent on depth. The deep currents, as the thermohaline circulation, are slow and depend on temperature and salinity gradients.

iii) Weather systems.– Low-pressure areas, specially tropical cyclons, accumulate and transport latent heat.

2.2.3 The effect of rotation on the atmospheric circulation

The rotation rate of the planet has a major role in the circulation patterns of the atmosphere (Section 5.1): larger rotation periods produce a large meridional scale of the stationary wave that produces equatorial jets (Edson et al., 2011), and slow rotating planets, like Venus and Titan exhibit superrotating winds. At superrotating regimes, the zonal wind has a greater angular momentum than the correspondent solid-body, instabilities in the mid-latitude jets produce planetary scale waves that transport angular momentum from this region to the equator, where they maintain a superrotating flow. In general, the phenomenon appears in a band at the equator and becomes inertially unstable at higher latitudes, depending on the rotation rate of

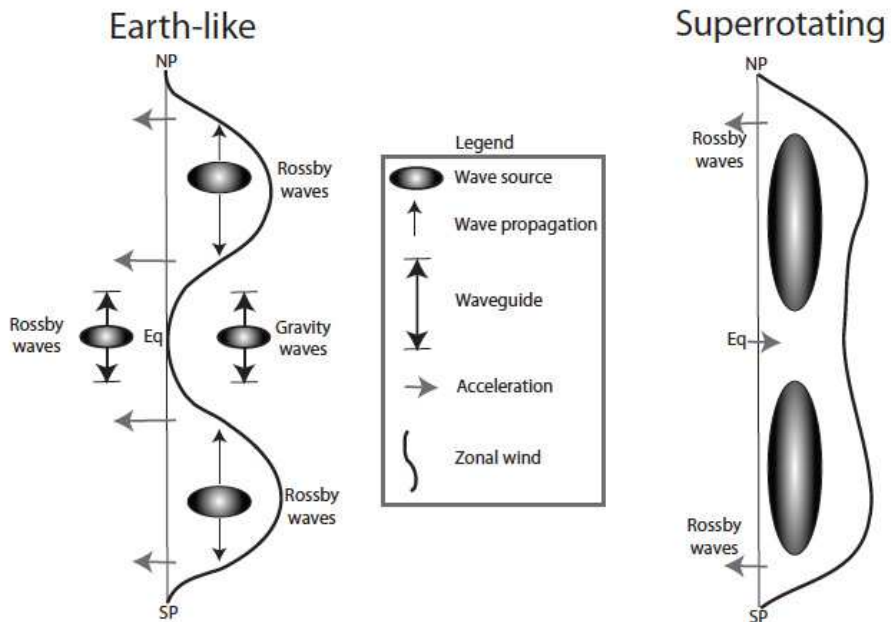

Figure 2.9 Schematic representation of eddy-mean-flow interaction in the Earth (left) and in a superrotating regime in Titan (right). From Mitchell & Vallis (2010).

the planet. Earth's troposphere does not show superrotation as it has easterly winds at the equator.

A mechanism that may lead to a superrotating state is a meridional transport of angular momentum to the equator by Rossby waves. A characteristic of these waves is that the momentum is transported in the opposite direction of their group velocity and may produce superrotation under certain conditions (Figure 2.9). In the Earth, Rossby waves are small, propagate from mid-latitudes towards the equator, then they break, decelerating the equatorial flow, and produce the easterly winds. However in the superrotating case, the scale of the baroclinic instability becomes larger than the planetary radius, a global disturbance is produced providing an eastward momentum at the equator that accelerates the zonal wind and as a result the superrotating westerly winds are generated (Mitchell & Vallis, 2010).

We evaluate three criteria to characterize superrotation on Earth-like planets:

i) The thermal Rossby number Ro_T.– A first criterion is to estimate the thermal Rossby number Ro_T, that express the force of the westerly wind as the balance between the inertial force due to the thermal (zonal) wind and the Coriolis force:

$$Ro_T = \frac{U_T}{2\Omega_r R_P} = \frac{R_{sp} T_S \Delta_T}{(2\Omega_r R_P)^2} \tag{2.14}$$

where U_T is the zonal wind velocity, Ω_r is the rotation rate of the planet, R_P is the radius of the planet, R_{sp} is the specific gas constant of dry air, T_S is the mean surface temperature, and $\Delta_T = 1. - T_{pole}/T_{equator}$ is the fractional meridional temperature gradient. Mitchell & Vallis (2010) show that the superrotation regime in Earth-like atmospheres arises when $Ro_T > 1$, although the superrotation and non-superrotating co-exist at Ro_T=1.3.

ii) The zonal wind velocity u_L.– A second method to evaluate superrotation is to calculate the condition of the zonal wind velocity to be in a superrotation state. Being $M_0 = \Omega R^2$ the angular momentum at the equator, in general using the thin shell approximation the zonal wind will at a certain latitude δ have an angular momentum M:

$$M = \Omega_r R_P^2 \cos^2 \delta + u R_P \cos \delta \tag{2.15}$$

A superrotating regime implies $u > u_0$, and then threshold zonal wind speed u_L is stablished as:

$$u_L = \frac{\Omega_r R_P \sin^2(\delta)}{\cos \delta} \tag{2.16}$$

iii) The Equatorial Rossby deformation length l_R.– A third parameter to delimit superrotation regimes is the Rossby radius of deformation, which gives us the length scale at which the effects of stratification and rotation balance under geostrophic

conditions (Coriolis and the horizontal pressure gradient forces are in equilibrium):

$$l_R = \frac{NH}{f} \tag{2.17}$$

where N is the Brunt–Väisäla frequency, H is the scale height, f is the Coriolis parameter, which can be written in terms of the rotation rate Ω_r and the latitude θ as $f = 2\Omega_r sen\theta$. Following the β-plane approximation, near the Equator f can be expressed as $f = f_0 + \beta y$, where $\beta = 2\Omega_r(cos\theta)/R_P$ and R_P is the radius of the planet, and the Rossby radius of deformation is given by (Chelton et al., 1998):

$$l_R = \sqrt{\frac{NH}{2\beta}} = \sqrt{\frac{NHR_P}{4\Omega_r}} \tag{2.18}$$

We can also define a dimensionless equatorial Rossby deformation length by comparing l_R with the radius of the planet:

$$L_R = \frac{l_R}{R_P} = \sqrt{\frac{NH}{4R_P\Omega_r}} \tag{2.19}$$

where R_P is the planetary radius. According to del Genio & Suozzo (1987), superrotation develops when the length scale of the perturbation, which is proportional to the Rossby deformation radius, is greater than the radius of the planet ($L_R > 1$).

The Earth's atmosphere can be considered as a dry stably stratified atmosphere up to 10 km, corresponding to the extension of the troposphere. The Brunt–Väisäla frequency is given by:

$$N^2 = \frac{g}{T}\left(\frac{g}{c_p} + \frac{dT}{dz}\right) \tag{2.20}$$

where c_p is the heat capacity of the air at constant pressure. Assuming a lineal atmosphere $T(z) = T_0 - az$, where $a = -dT/dz$ is the lapse rate, and replacing the scale height by $H = RT_S/m_a g$, where R is the ideal gas constant, T_S is the mean surface temperature, m_a is the molecular mass of the air, and g is the gravitational acceleration, L_R can be written as:

$$L_R = \sqrt{\frac{R}{4R_P\Omega_r m_a}\left(\frac{g}{c_p} - a\right)} \tag{2.21}$$

where the lapse rate a is obtained by integrating the barometric formula for a lineal atmosphere:

$$a = \frac{-g \ln (T_z/T_0)}{R \ln (p_z/p_0)} \tag{2.22}$$

where p_0 and T_0 are the surface pressure and temperature, and p_z and T_z are the pressure and temperature at an altitude z.

This three criteria are considered in Section 5.2 (Table 5.3) and Section 6.2 (Table 6.3) in order to identify superrotation regimes in our set of Earth-like planets.

2.3 Analysis of the signal

The analysis of the time series is done in three steps: the study of the origins of the variability of the signal (diurnal cycle, rotational movement, seasonality, weather patterns, etc...) according to the planetary characteristics; the retrieval of the rotation period by autocorrelation and the analysis of the average rotation light curves. The first is explained with the results in Section 4.2 for the Earth (NASA-SRB data), in Section 5.3 for the set of terrestrial planets, and in Section 6.3 for the set of aquaplanets. Here we explain the method of autocorrelation and the construction of the longitudinal curves.

2.3.1 Autocorrelation

The analysis of the cross-correlation of the time series with itself or autocorrelation, shown in Figure 2.10 (left), is a technique that allows to determine the rotation period of the planet and the lifetime of the cloud structures. The autocorrelation A can be computed as:

$$A(L) = \frac{\sum_{k=0}^{N-L-1} \left(F(k\Delta t) - \overline{F}\right) \left(F((k+L)\Delta t) - \overline{F}\right)}{\sum_{k=0}^{N-1} \left(F(k\Delta t) - \overline{F}\right)^2}, \tag{2.23}$$

where L is the time lag in number of 3 hr points, N is the total number of points in the time series, and $\overline{F}$ is the mean flux. The autocorrelation is maximum

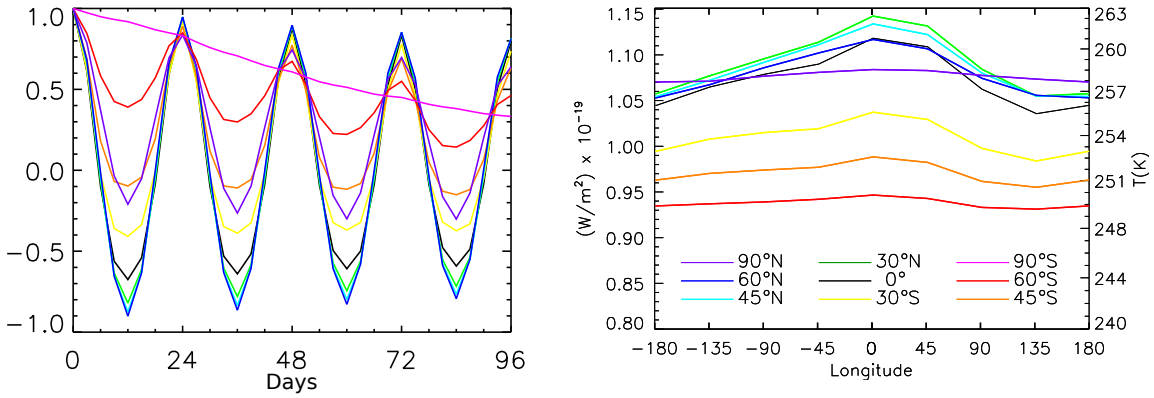

Figure 2.10 *Left:* Autocorrelation of the time series in Fig. 2.3 during northern summer. *Right:* Correspondent rotation light curve. Colours correspond to the latitude of the sub-observer point.

when values are similar within a time lag distance and it is sampled according to the time resolution. This method was chosen before the Fourier Transform to avoid the harmonics of the rotational period. The duration of the statistically significant peaks in the autocorrelated time series can give us an estimation of the lifetime of the cloud structures, typically of around one week for Earth clouds (Pallé et al., 2008).

The use of this method is limited by three factors: the number of periods contained in the series, the time resolution, and climatic effects over the signal. In order to get good statistics on the results, the observation needs to cover a large number of periods. It is also important to have an adequate time resolution to obtain a good sampling of the periodicity, if the latter is not a multiple of the time resolution, there is a longitudinal angle phase $\Delta\phi$ between the real period and the measured period that is cumulative over time, and as a consequence, the longer the time considered, the worser the autocorrelation. Some climate effects, as the seasonal flux change or the random effect of clouds, have an influence on the autocorrelation function and they are also cumulative. In our case we have made the best compromise between these factors and found that the most accurate results are obtained with a length of the series of $\sim$10 days. The autocorrelation of the Earth (NASA-SRB data) is

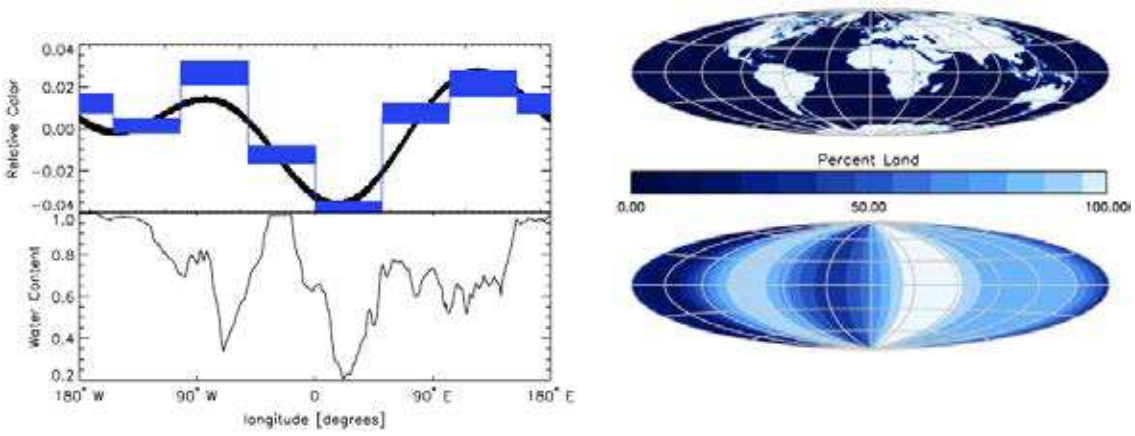

FIGURE 2.11 *Left:* Longitudinal curves of the oceanic distribution on Earth: N-slice model (blue) and sinusoidal (black) for June EPOXI simulations (top panel) and MODIS cloud-free, equator weighted observations (bottom panel). *Right:* Land distributions for a MODIS map (top panel) and an June EPOXI longitudinal map. (From Cowan et al. 2009).

discussed in Section 4.3 (Fig. 4.3) and the results for our set of planets (LMDZ data) are presented in Section 5.4 (Table 5.5) and Section 6.4 (Table 6.5).

2.3.2 Rotation light curves

Once the rotation period is identified, the observer can produce a typical rotation light curve by folding the time series obtained during weeks or months over the rotation period Figure 2.10 (right). The average flux obtained at each fraction of the period, according with the time resolution of the data, constitutes the points of the final rotational light curve. This process averages out the random cloud variability, the effect of the clouds disappears averaging over long periods of time whereas the strongest features of the emission prevail. The observer can plot this average rotation light curve as a function of an arbitrary longitude (in our case the longitude that we have chosen is the conventional geographic longitude for commodity), and the shape of this rotational light curve can then reveal brighter/fainter areas of the planet

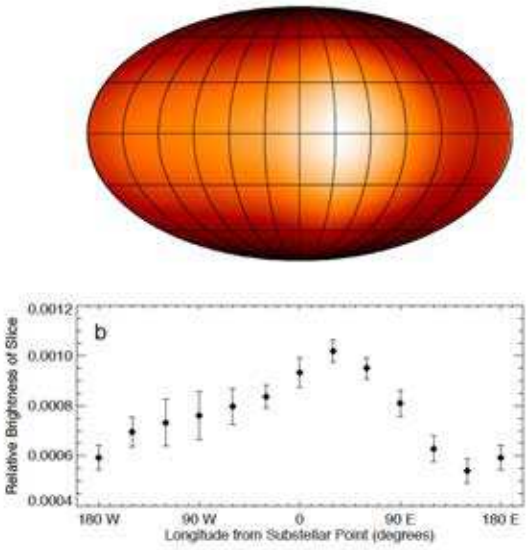

FIGURE 2.12 A map of the day-night contrast of the extrasolar planet HD 189733b (from Knutson et al., 2007).

distributed in longitude. Several authors (Rutten, 1996; Knutson et al., 2007; Cowan & Agol, 2008; Cowan et al., 2009) have reproduced exoplanet longitudinal maps by similar methods (Figure 2.12). We present the longitudinal light curves of the Earth (NASA-SRB data) in Section 4.4 (Fig. 4.3 and Fig. 4.4), those of our set of terrestrial planets in Section 5.5 (Fig. 5.18), and those of our set of aquaplanets in Section 6.5 (Fig. 6.12).

2.4 Summary

We have built a geometrical model that can simulate the point-like emission signal of an Earth-like planet received by an observer at any geometry and distance. By the comparison of mean limb darkening models and for the sake of simplicity we conclude that the Lambertian approximation is applicable on the simulation of the thermal emission of the Earth-like planets of our set. Our model can also calculate the global characteristics of the planet as the effective temperature, the Bond albedo,

the greenhouse parameter, or the cloud radiative forcing to study the climate and to analyze the influence of the variation of these parameters on the signal. In addition, by the further analysis of the light curves, we can retrieve certain parameters such as the rotation rate, the albedo and the effective temperature. We can also built longitudinal maps to reveal warm and cold regions of the planet and include the effect of natural satellites.